

Vortex Tunneling and Critical State in an Oxide Heterostructure

Jordan T. McCourt,^{1,*} Ryan Henderson,¹ John Chiles,¹ Chun-Chia Chen,¹
Shama,¹ Divine Kumah,¹ Vadim Geshkenbein,² and Gleb Finkelstein^{1,†}

¹*Department of Physics, Duke University, Durham, NC 27708, USA*

²*Institute for Theoretical Physics, ETH Zurich, Zurich, Switzerland*

(Dated: February 24, 2026)

Two-dimensional superconductors offer an excellent platform for the study of vortex matter due to their low superfluid stiffness and inability to effectively screen applied magnetic fields. Here we explore vortices in a two-dimensional superconductor formed at the surface of the complex oxide KTaO_3 . Multiple regimes of vortex-mediated transport are identified and studied, revealing switching behaviour attributed to nucleation of individual vortices. Analysis of this regime allows us to identify the quantum tunneling of vortices, which transitions to thermally activated behaviour at elevated temperatures. Magnetic field dependence reveals rich histograms of the switching currents which we attribute to different configurations of pinned vortices.

INTRODUCTION

Two-dimensional superconductors (2D) formed at complex oxide interfaces and van der Waals materials have attracted intense interest because they realize regimes fundamentally different from those found in conventional superconducting thin films. In these systems, superconductivity emerges in a truly two-dimensional environment where carrier density, spinorbit coupling, and interaction strength can be tuned in situ [1–3]. This tunability, together with reduced dimensionality, enhances the role of phase fluctuations, broken symmetries, and electronic correlations, enabling access to superconducting states that are difficult or impossible to achieve in bulk materials. As a result, 2D superconductors provide a versatile platform for exploring unconventional pairing, quantum phase transitions, and the interplay between superconductivity, topology, and other competing electronic orders.

In 2D superconductors with thickness d much less than the London penetration depth λ , the characteristic length determining the screening of magnetic field is the Pearl length $\Lambda = \frac{2\lambda^2}{d}$ [4]. This scale could be as large as millimeters, which greatly exceeds the typical sample width W , as a result, the superconductor is unable to screen the applied perpendicular magnetic field, and $B \approx H$. In this regime, the effects of surface nucleation and bulk pinning of vortices will dominate the transport properties. This regime is discussed in the recent paper [5], which considers a current-carrying superconducting strip in magnetic field.

At very small magnetic fields (Meissner state) the field-induced diamagnetic currents on the two sides of the strip are either added to or subtracted from the externally applied bias current. As a result, the critical current

density is reached on one side of the strip at a lower bias current compared to zero field. The measured critical current of the strip thus decreases linearly with the field, $I_C(H) = I_C(0) \left(1 - \frac{|H|}{H_S}\right)$. Here, $I_C(0)$ is the critical current at zero field, and H_S is the maximal field at which the Meissner state could exist at zero applied current.

While at small magnetic fields the current density at I_C is too high to allow for the vortex pinning in the bulk, above a characteristic field H^* , the critical current density drops sufficiently to allow for the vortices to be pinned. The superconductor enters a critical state in which vortices can be present in the bulk, and $I_C(H)$ is increased to $I_P \left(1 + \frac{(H^*)^2}{|H|H_P}\right)$ [5], (here, I_P and H_P are parameters that depend on the vortex pinning). The deviation from the linear I_C vs H dependence and the onset of the characteristic $1/H$ dependence therefore signals the presence of vortices close to I_C .

In this paper, we explore the regimes where a small number of vortices, possibly zero or one, are present in the superconducting constriction. We demonstrate the regimes corresponding to continuous vortex flow, and switching controlled by nucleation of a single vortex. In the latter regime, we find the temperature-independent saturation of the nucleation rate, which we associate with the macroscopic quantum tunneling of the vortex.

CRITICAL CURRENT AND FIELD DEPENDENCE

The samples in this work were formed by depositing 7 nm of Al on a KTaO_3 (111) substrate. The Al layer is oxidized thereby reducing the KTaO_3 layer, as a result forming a 2-dimensional electron gas (2DEG) at the $\text{AlO}_x/\text{KTaO}_3$ interface [7]. The carrier density of the 2DEG is $n \approx 8 \times 10^{13} \text{ cm}^{-2}$ with a mobility of $\approx 90 \text{ cm}^2/\text{Vs}$ at cryogenic temperatures. The critical temperature is 1.3 K and the critical perpendicular magnetic field 0.6 T. Using electron beam lithography and

* jordan.mccourt@duke.edu

† gleb@duke.edu

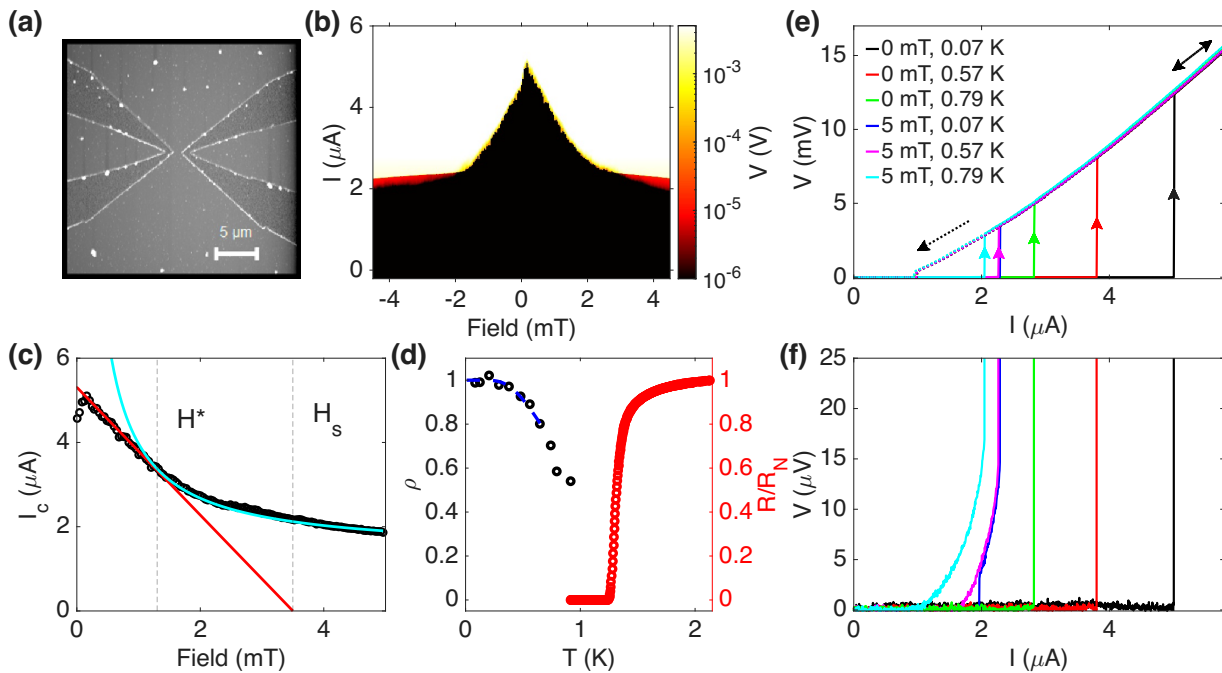


FIG. 1. (a) An AFM image of constriction A studied here and in Figure 4. The light grey region denotes the conductive channel, whilst the darker regions denote the area etched and left insulating. The conductive regions around the constriction were intended to be used as gates in the style of our previous work [6], but were left unused here. (b) Map of voltage across the constriction as a function of bias current I and perpendicular magnetic field B . Note the logarithmic colour scale. (c) Extracted I_C (circles) overlaid with curves corresponding to expressions from [5]. Due to the small asymmetry of the junction (Supplementary Figure 6) the max I_C is shifted from zero field. (d) Relative superfluid density, ρ (black circles) with fit (blue dotted line) and the resistance of the film, $R(T)$, normalized to the normal state resistance, R_N (red circles). ρ is obtained from the slope dI_C/dB extracted in the Meissner regime at different temperatures (supplementary Figure 9). These slopes are then normalized to dI_C/dB measured at the base temperature in panels (b) and (c). (e) IV curves for a range of temperatures at zero field and 5 mT. Solid and dashed lines correspond to IV sweeps with increasing and decreasing bias, respectively. Note that the switching currents depend on T and B , while the retrapping currents and the $I - V$ curves in the high voltage state do not. These observations indicate that on the high voltage branch some part of the sample enters a normal state, which is then sustained by the dissipated power. (f) Same curves as in panel (e) on a much smaller voltage scale. The curves measured at finite field display an initial μV -scale segment, which we associate with the vortex flow.

reactive ion etching, we pattern $1 \mu\text{m}$ wide hourglass-shaped constrictions in the plane of the 2DEG, Figure 1a. Two devices are presented in the main text, referred to as devices A (Figures 1, 4) and B (Figures 2, 3).

Since the largest current density along the edge is concentrated at the constriction, we expect it to dominate the transition from the superconducting state. Figure 1b shows the voltage across the constriction, V , as a function of the applied current, I , and perpendicular magnetic field, B . We average multiple sweeps of I for a given field and define I_C when the voltage exceeds $0.5 \mu\text{V}$ (the extracted I_C is not sensitive to this threshold). In Figure 1c, we plot $I_C(B)$ (circles) overlaid with fits to the theoretical predictions in the Meissner and mixed states [5], showing good agreement with the experimental results. The linear behaviour of the Meissner regime is clearly visible, before smoothly interpolating to the mixed regime when $B \approx 1.3 \text{ mT}$. Similar behaviour of I_C has been observed in thin metal films [8] and novel 2D superconductors with $W \ll \Lambda$ [9].

An asymmetry in the surface barrier can result in a slight shift of the triangle-shaped current maximum away from zero B [5]. This results in a superconducting diode effect at finite field, as recently demonstrated in KTaO_3 -based devices [10, 11] and other materials [12]. We show this behavior in our samples in the appendix, Figure 7. With careful engineering of the surface barrier, KTaO_3 could act as a versatile platform for novel superconducting electronics when combined with the gate-tunability of the superconducting state [6].

The slope of $I_C(B)$ in the Meissner regime allows one to extract the Pearl length Λ from $\frac{dI_C}{dB} = -\frac{W^2}{\mu_0 \Lambda}$ [5], which we estimate as $\Lambda \approx 1 \text{ nm}$. While this equation is exact for a superconducting strip, we expect it to be correct, up to a geometric factor of order 1, in the case of a constriction of width W . From Λ , we directly calculate the superfluid stiffness, $J_s = \frac{\hbar^2}{2\mu_0 e^2 \Lambda} \approx 15 \text{ K}$, and kinetic inductance of $L_K = \frac{\hbar^2}{4e^2 J_s} \approx 0.5 \text{ nH}$ (both at the base temperature). These quantities agree with the range found

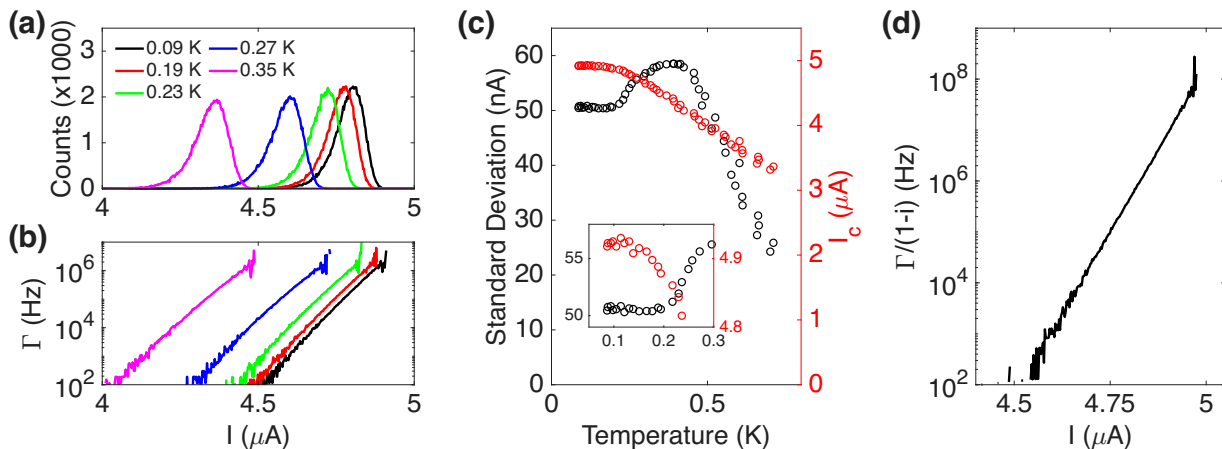


FIG. 2. (a) Histograms of switching currents at zero field and several temperatures for device B. (b) Escape rate extracted from the histograms in panel (a). (c) Standard deviation of the switching current distributions and critical current over a range of temperatures. (d) Scaling of the escape rate divided by the current-dependent prefactor (see text), demonstrating the exponential dependence on the applied current.

in other KTaO_3 samples [7, 13, 14]. We measure multiple $I_C(B)$ curves at different temperatures in the supplementary Figures 8 and 9. As $\Lambda \propto 1/n_s$ where n_s is the Cooper pair density, we can plot the fraction of the superconducting electrons, $\rho(T)$ in Figure 1d. We fit it with the low-temperature expression for an isotropic s-wave superconductor at low temperatures [15], from which we find the gap at $T = 0$ of $\Delta_0 \approx 180 \mu\text{eV}$, consistent with the transition temperature of about 1.3 K.

Next, in Figure 1e we compare the $I - V$ curves at $B = 0$ and 5 mT, at three temperatures. All the curves show a similar behavior: starting at zero current, they abruptly switch from a low voltage state ($V < 100 \mu\text{V}$) to the high voltage state ($V \sim 10 \text{ mV}$) at the “switching” current. Due to the high dissipated power of several tens of nW, it is likely that in this regime a large portion of the 2DEG surrounding the constriction becomes normal.

Upon reversal of the current sweep, the curves transition from the high to the low voltage state at the “retrapping” current. Note that while the switching currents strongly depend on the temperature and magnetic field, as expected from Figure 1c, the retrapping current is nearly independent of the temperature or the field (in the few mT range). Furthermore, in the high resistance state the voltage also does not depend on B and T , Figure 1e. This further supports the interpretation of the high-voltage state as the normal state sustained by Joule heating.

We now zoom in by 3 orders of magnitude in voltage to the low voltage state. Figure 1f shows the same IV curves as in Figure 1e (upward ramp only), but on the μV scale rather than the mV scale. Here, we observe different behaviors at zero (or very small) B vs larger values of B . Namely, at $B = 0$, the curves switch from the noise floor (less than $1 \mu\text{V}$) straight to the high voltage state.

At $B = 5 \text{ mT}$, there exists a low voltage regime with V in the range of a few μV (this regime is visible in the map of Figure 1b as a red sliver at the transition between the black and white regions). We argue that this regime corresponds to flux flow, and return to it later in Figure 4. For now, we turn our attention to the direct switch from zero resistance to the normal state at zero or very small magnetic field.

SWITCHING STATISTICS AND RATES

We are now interested in exploring the nucleation of vortices at the edge of the constriction. We first present measurements at zero field (Figure 2), so that the pinned vortices should be absent. Here, and in Figure 3, we work with device B, nominally identical to device A studied in Figures 1 and 4.

Upon multiple sweeps of the $I - V$ curves, the transition from the zero to mV scale voltage occurs at slightly different values of bias current. We collect the statistics of the switching events from multiple linear current sweeps [16]. Following the nucleation of the vortex, the $I - V$ curve switches to the normal state. For each sweep, the value of the switching current I_S is recorded, and the resulting histograms of I_S are shown in Figure 2a. Clearly, the average I_S increases as temperature decreases, before the distribution saturates at the lowest temperatures. Using established methods [16], we can convert the switching histogram to the average switching rate, Γ , plotted in Figure 2b with the same horizontal axis.

In Figure 2c, we plot the standard deviation (i.e. the width) of the distribution, and the maximal switching current, identified by the sharp drop-off of the histograms at their upper end. The three regimes familiar from the

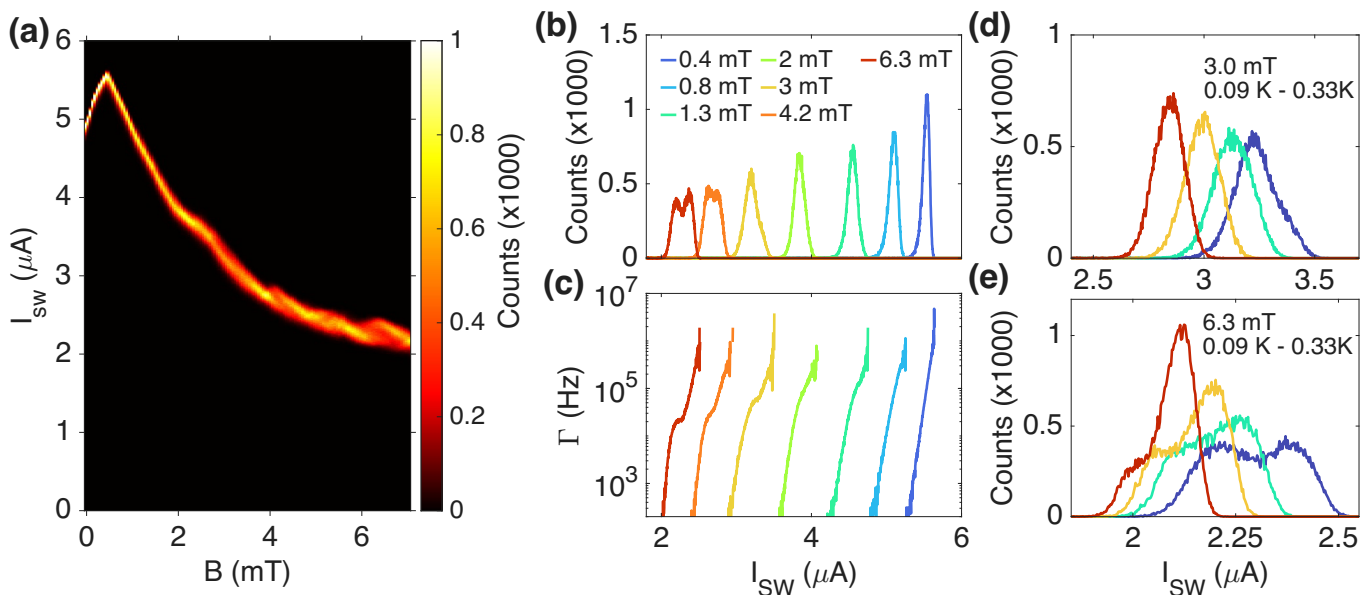


FIG. 3. (a) Heat map of multiple switching histograms like in Figure 2a, plotted as a function of B at 0.09 K. (b) Histograms at various fields corresponding to the vertical cuts of panel (a). At $B \approx 1$ mT the histograms lose their asymmetric shape before transitioning to distributions with multiple peaks. (c) Escape rates calculated from histograms in panel (b) under the assumption of a single population of the initial states. (d,e) Histograms of switching currents at 3.0 mT (top) and 6.3 mT (bottom) for 0.09 K (blue), 0.24 K, 0.29 K and 0.33 K (red).

Josephson junctions are clearly visible: the phase diffusion ($T \gtrsim 0.45$ K), the thermally activated switching with the histogram width growing with temperature (0.2 K $\lesssim T \lesssim 0.4$ K) [17], and the low-temperature saturation ($T \lesssim 0.15$ K).

We are particularly interested in the third regime, potentially corresponding to the macroscopic quantum tunneling of vortices from the nucleation site at the edge of the constriction. The quantum tunneling of a vortex is fundamentally distinct from the macroscopic quantum tunneling observed in underdamped Josephson junctions [18]. While both phenomena can be formulated as tunneling of a particle coupled to dissipative environment, vortex tunneling corresponds to the real-space motion of a topological excitation across a barrier. Furthermore, the motion of the vortex may be expected to be overdamped. Signs of the macroscopic quantum tunneling of vortices have been reported in the $I - V$ curves of High T_C films [19], for Josephson vortices in annular junctions [20], and very recently based on the vortex entry and exit rates in magic angle twisted graphene [21].

We expect the rate of this process to scale as $\Gamma \propto (1 - i) \exp(-\alpha(1 - i))$, where α is a constant, $i = I/I_C$ and I_C is the “true critical current” at which the energy barrier for vortex nucleation vanishes [22]. The expression above corresponds to tunneling with strong dissipation, expected in the case of vortices and similar to the behavior of a Josephson junction in the overdamped regime. The slight deviation of the switching rate from the linear slope on the log-linear plot in Figure 2b can

be adequately accounted for by the prefactor $1 - i$. In Figure 2d, we plot $\Gamma/(1 - i)$ with $I_C = 5.05 \mu\text{A}$, which clearly works well.

Next, we explore the switching process as a function of the magnetic field. Figure 3a shows the map made of multiple switching histograms as a function of the magnetic field. The μV -scale flux-flow regime we have encountered in Figure 1f does not set in until $B \sim 12$ mT in this constriction (supplementary Figure 11) and all the switching events in Figure 3a take the system from zero to the normal state. The individual histograms corresponding to select vertical cuts of the map are shown in Figure 3b, and the calculated switching rates in Figure 3c. The measurement shown in Figure 2 corresponds to the $B = 0$ curve (dark blue).

As we move away from $B = 0.4$ mT, which corresponds to the highest critical current, we find the curves deviate further and further from the typical Gumbel distribution seen in Figure 2a: they become less asymmetric and eventually develop sub-peaks. The corresponding calculated escape rates demonstrate two offset segments with a similar slope (see the red curve at $B = 6.3$ mT). Figure 3a shows that these peak doublings correspond to transitions between different branches on the map, with the lower current branches waning as the field increases, while being replaced by the upper branches.

We argue that these branches correspond to the different vortex configurations – the next branch adds one vortex (or more) to the constriction, which reduces the diamagnetic current at the edge, thereby increasing the

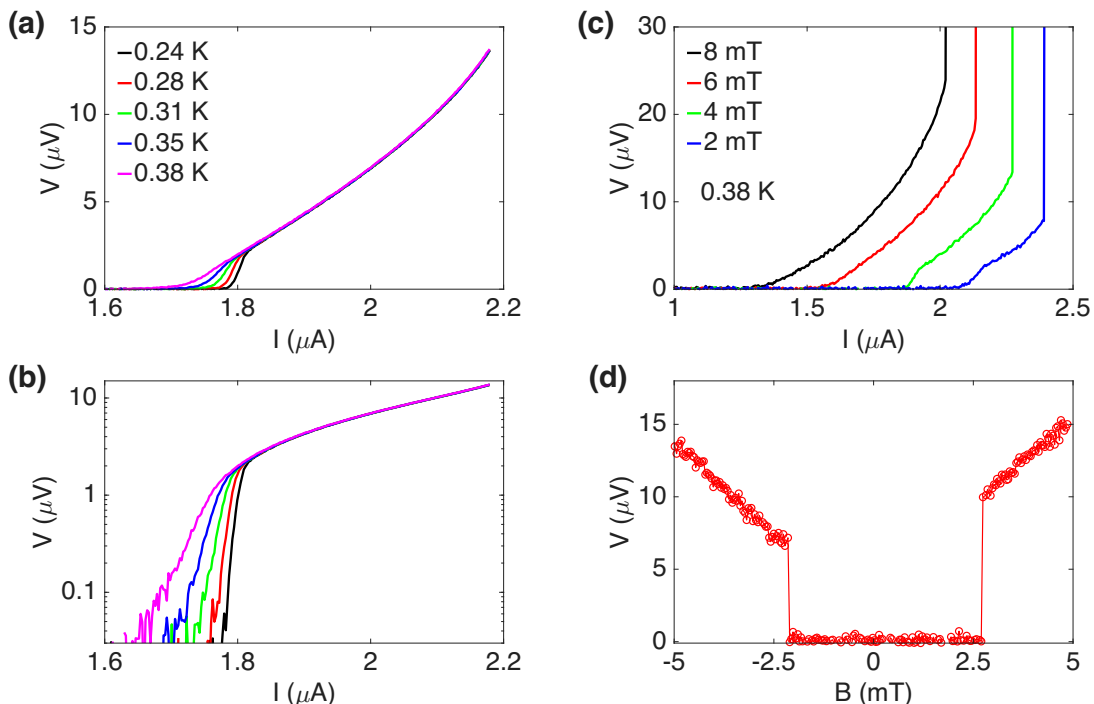


FIG. 4. (a) $I - V$ curves in the μV regime measured in device A for a range of temperatures $T \gtrsim 0.24\text{K}$ at $B = 5.6\text{mT}$. Note that the curves are temperature-independent for $I \gtrsim 1.82\mu\text{A}$. (b) The same data from (a) plotted on a logarithmic voltage scale, demonstrating the exponential temperature-dependent tail. (c) $I - V$ curves at several values of B showing the vortex flow regime and the jump to the normal state. The voltage at the end point of the vortex flow regime is extracted for the next panel. (d) Voltage measured immediately prior to switching from the vortex flow (μV) regime to the normal (mV) regime, plotted as a function of magnetic field.

critical current. The presence of the two peaks in the histogram corresponds to two distinct populations: for a given sweep, the number of vortices in the constriction is likely fixed following the cooling off following the previous sweep. We note that in the case when two sub-populations are present, one cannot rely on the values of the switching rate in Figure 3c, extracted using the expressions in Ref. [16], which assumes a single population. As the temperature increases, the finite-field histograms may begin to recover some of the asymmetry (Figure 3d), or, in some cases, one peak may come to dominate the other (Figure 3e). This behavior suggests that the distinct populations contributing to the measured histograms evolve on different temperature scales.

I-V CURVES: VORTEX FLOW AND CREEP

We now return to the sample shown in Figure 1 and discuss the $I - V$ curves at finite field in more detail.

First, we plot the low-voltage regime for $B = 5.6\text{mT}$ at several temperatures in Figure 4a. The same curves are plotted on a logarithmic voltage scale in Figure 4b. We observe that the lower end of the IV curves (below $I = 1.8\mu\text{A}$) appears linear on the log-linear plot, indicating an exponential dependence of the voltage on bias

current, with a slope that depends on temperature. In contrast, the higher end of this low-voltage regime (above $\sim 1.82\mu\text{A}$) does not depend on temperature, and here multiple curves coalesce. Clearly, this is not the normal state, because the voltage here is ~ 1000 times lower than that in the high-voltage state of Figure 1e.

We tentatively attribute this temperature-independent regime (above $\sim 1.82\mu\text{A}$) to the vortex flow, in which the vortices are continuously crossing the constriction. Given the dimensions of the constriction and the magnitude of the field, we estimate that the number of vortices present in the constriction at a given time is of the order of one. Each time a vortex crosses the constriction results in a voltage pulse of $\int V dt = h/2e$. The measured voltage is equal to the average of the pulses, which is therefore proportional to the average velocity of the vortices. This consideration allows us to estimate that on average a vortex crosses the constriction once every 0.2 ns, corresponding to the velocity of 5 km/sec if only one vortex is present at a given time. This scale, and even higher velocities have been previously reported [23].

We now turn to the lower end of the curves in Figure 4a and Figure 4b (below $I = 1.8\mu\text{A}$). We speculate that the voltage in this regime is limited by the rate at which vortices are either nucleated at the edge of the constriction or depinned in the bulk. Once they start moving, the

vortices cross the constriction relatively fast, so that the measured voltage is proportional to the rate of the depinning or nucleation events, which in turn depends on temperature. Notably, these rates are suppressed at low temperature, and below $T \sim 200$ mK, the exponential tail of the $I - V$ curves disappears being replaced by stochastic switching from zero straight to the flux flow regime (supplementary Figure 10).

The vortex flow regime is bound on the upper end by an abrupt switching to the normal state. In Figure 4c, we show several such jumps for four values of magnetic field. Unlike the switching from the zero-voltage state, this jump occurs at the same value of current upon multiple current sweeps – see the dark blue and magenta curves in Figure 1f, measured at $T = 0.07$ and 0.57 K.

We speculate that at the end point of the vortex flow regime, an instability develops because the viscous drag force acting on the vortices reaches its maximal possible value. (See Ref. [24] for a review of the possible mechanisms.) The voltage at that point is found to be proportional to the applied magnetic field, as shown in Figure 4d.

The critical current for this instability is only weakly dependent on magnetic field, see the red-white boundary in Figure 1b. Since at small B the vortex nucleation threshold occurs at higher currents, the flux flow regime disappears below a certain field, and the system switches directly from the zero voltage to the normal state. This occurs for $|B| \lesssim 2$ mT for the first sample (Figure 1b) and $B \lesssim 10$ mT for the second sample (Figure 11a).

CONCLUSION

In this paper, we identify and explore several distinct regimes:

In the mixed state at finite field, we observe the regime in which the $I - V$ curves are (nearly) independent of temperature but strongly depend on the magnetic field. We argue that in this regime a few, and possibly just one vortex continuously shuttles across the constriction.

For smaller values of current, and elevated temperatures ($T \gtrsim 250$ mK) the voltage is found to depend exponentially on the current, and the slope of $\log V$ vs I depends on temperature. Here, the rate of vortex crossing the constriction is limited by their nucleation at the edge or depinning from the bulk.

Finally, we study the nucleation of the vortices at zero magnetic field as a function of applied bias. We measure the dependence of the escape rate on the proximity to the critical current I_C , which follows the semiclassical dependence for tunneling with a strong dissipation.

Overall, we find that the superconducting state at the interface of AlO_x and KTaO_3 represents a very promising playground for exploring the vortex dynamics in a 2D superconductor.

ACKNOWLEDGMENTS

We appreciate fruitful discussions with Filippo Gaggioli. J.T.M. thanks Stephen Teitworth for insightful discussions regarding tunneling scaling.

Sample fabrication by R.H. and J.T.M., transport measurements by J.T.M., J.C. and C.C. and data analysis by J.T.M. and G.F. were supported by the National Science Foundation grant DMR-2327535. Crystal synthesis by D.K. and S. were supported by the U.S. National Science Foundation under Grant No. NSF DMR-2324174. Sample fabrication by R.H. and J.T.M. was performed in part at the Duke University Shared Materials Instrumentation Facility (SMIF), a member of the North Carolina Research Triangle Nanotechnology Network (RTNN), which is supported by the National Science Foundation (award number ECCS-2025064) as part of the National Nanotechnology Coordinated Infrastructure (NNCI).

-
- [1] L. Balents, C. R. Dean, D. K. Efetov, and A. F. Young, Superconductivity and strong correlations in moiré flat bands, *Nature Physics* **16**, 725 (2020).
 - [2] H. Y. Hwang, Y. Iwasa, M. Kawasaki, B. Keimer, N. Nagao, and Y. Tokura, Emergent phenomena at oxide interfaces, *Nature Materials* **11**, 103 (2012).
 - [3] P. Zubko, S. Gariglio, M. Gabay, P. Ghosez, and J.-M. Triscone, *Interface Physics in Complex Oxide Heterostructures*, Annual Review of Condensed Matter Physics **2**, 141 (2011).
 - [4] J. Pearl, Current distribution in superconducting films carrying quantized fluxoids, *Applied Physics Letters* **5**, 65 (1964).
 - [5] F. Gaggioli, G. Blatter, K. S. Novoselov, and V. B. Geshkenbein, Superconductivity in atomically thin films: Two-dimensional critical state model, *Physical Review Research* **6**, 023190 (2024).
 - [6] J. T. McCourt, E. G. Arnault, M. Bakshi, S. J. Poage, S. Salmani-Rezaie, K. Ahadi, D. Kumah, and G. Finkelstein, Electrostatic Control of Quantum Phases in KTaO_3 -Based Planar Constrictions, *Nano Letters* **25**, 16091 (2025).
 - [7] S. Mallik, G. C. Mnard, G. Saz, H. Witt, J. Lesueur, A. Gloter, L. Benfatto, M. Bibes, and N. Bergeal, Superfluid stiffness of a KTaO_3 -based two-dimensional electron gas, *Nature Communications* **13**, 4625 (2022).
 - [8] B. L. T. Plourde, D. J. Van Harlingen, D. Y. Vodolazov, R. Besseling, M. B. S. Hesselberth, and P. H. Kes, Influence of edge barriers on vortex dynamics in thin weak-pinning superconducting strips, *Physical Review B* **64**, 014503 (2001).
 - [9] M. Perego, C. Galante Agero, A. Mestre Tor, E. Portols,

- A. O. Denisov, T. Taniguchi, K. Watanabe, F. Gaggioli, V. Geshkenbein, G. Blatter, T. Ihn, and K. Ensslin, Experimental detection of vortices in magic-angle graphene, *Nature Communications* **16**, 10259 (2025).
- [10] Y. Wang, W. Pan, M. Zhang, and Y. Xie, KTaO₃-Based Editable Superconducting Diode, *Chinese Physics Letters* **43**, 010713 (2025).
- [11] M. Yu, J. Kim, A. Omran, Z. Li, J. Yang, S. Biswas, C.-B. Eom, D. Pekker, P. Irvin, and J. Levy, KTaO₃-Based Supercurrent Diode, *Nano Letters* 10.1021/acs.nanolett.5c05590 (2026).
- [12] Y. Hou, F. Nichele, H. Chi, A. Lodesani, Y. Wu, M. F. Ritter, D. Haxell, M. Davydova, S. Ili, O. Glezakou-Elbert, A. Varambally, F. S. Bergeret, A. Kamra, L. Fu, P. A. Lee, and J. S. Moodera, Ubiquitous Superconducting Diode Effect in Superconductor Thin Films, *Physical Review Letters* **131**, 027001 (2023).
- [13] M. Yu, N. Hougland, Q. Du, J. Yang, S. Biswas, R. Ramachandran, D. Yang, A. Bhattacharya, D. Pekker, P. Irvin, and J. Levy, Sketched Nanoscale KTaO₃-Based Superconducting Quantum Interference Device, *Physical Review X* **15**, 011037 (2025).
- [14] J. Yang, A. Imamovic, X. Li, X. Zhou, J. Pearson, C. Liu, U. Welp, A. Higginbotham, J. S. Jiang, D. Jin, M. R. Norman, and A. Bhattacharya, Tuning Kinetic Inductance with Doping in Superconducting Electron Gases at the KTaO₃ (111) Interface, *Nano Letters* 10.1021/acs.nanolett.4c06029 (2025).
- [15] R. Prozorov and R. W. Giannetta, Magnetic penetration depth in unconventional superconductors, *Superconductor Science and Technology* **19**, R41 (2006).
- [16] T. A. Fulton and L. N. Dunkleberger, Lifetime of the zero-voltage state in Josephson tunnel junctions, *Physical Review B* **9**, 4760 (1974).
- [17] J. Kurkijärvi, Intrinsic Fluctuations in a Superconducting Ring Closed with a Josephson Junction, *Physical Review B* **6**, 832 (1972).
- [18] J. Clarke, A. N. Cleland, M. H. Devoret, D. Esteve, and J. M. Martinis, Quantum Mechanics of a Macroscopic Variable: The Phase Difference of a Josephson Junction, *Science* **239**, 992 (1988).
- [19] F. Tafuri, J. R. Kirtley, D. Born, D. Stornaiuolo, P. G. Medaglia, P. Orgiani, G. Balestrino, and V. G. Kogan, Dissipation in ultra-thin current-carrying superconducting bridges; evidence for quantum tunneling of Pearl vortices, *Europhysics Letters* **73**, 948 (2006).
- [20] A. Wallraff, A. Lukashenko, J. Lisenfeld, A. Kemp, M. V. Fistul, Y. Koval, and A. V. Ustinov, Quantum dynamics of a single vortex, *Nature* **425**, 155 (2003).
- [21] M. Perego, P. Koopmann, C. G. Agero, A. M. Tora', A. O. Denisov, T. Taniguchi, K. Watanabe, V. Geshkenbein, G. Blatter, T. Ihn, and K. Ensslin, Pearl-Vortex Tunneling in Magic-Angle Twisted Graphene (2026).
- [22] U. Weiss, *Quantum Dissipative Systems (Fifth Edition)* (WSPC, 2021).
- [23] L. Embon, Y. Anahory, L. Jeli, E. O. Lachman, Y. Myasoedov, M. E. Huber, G. P. Mikitik, A. V. Silhanek, M. V. Miloevi, A. Gurevich, and E. Zeldov, Imaging of superfast dynamics and flow instabilities of superconducting vortices, *Nature Communications* **8**, 85 (2017).
- [24] O. Dobrovolskiy, Fast dynamics of vortices in superconductors, *Encyclopedia of Condensed Matter Physics (Second Edition)*, 735 (2024).

Appendix

Time-reversal symmetry

Figure 5 compares the voltage maps of device A for positive and negative current sweep directions. We present the second map flipping the direction of the current and field axes. Clearly, reversing the sign of I , V , and B results in very similar maps. This indicates that any intrinsic magnetism associated with d-orbitals of the Ta ions is negligible in this sample.

Figure 6 shows similar maps for device B. Here, the axes are not inverted, and the time-reversal symmetry is demonstrated by the 180° rotation symmetry of the two maps measured for the up and down current sweep directions. Because of the asymmetry in the device, it can be seen how a diode effect may occur at finite field.

Superconducting Diode Effect

In Figure 7, we display the superconducting diode efficiency (η) extracted directly from Figure 5 and at various temperatures (left). The efficiency is defined as $\eta = \frac{I_{C+} - |I_{C-}|}{I_{C+} + |I_{C-}|}$, where I_{C+} and I_{C-} are the critical current at positive and negative bias sweep respectively. The right plot displays η for the third constriction (C) made simultaneously with device A. It appears to have a greater surface barrier asymmetry, and as a result a larger diode efficiency. The diode effect decreases with temperature but still persists even close to T_C .

Bias-field Characteristics at Various Temperatures

Figure 8 shows voltage maps of device A at different temperatures from 0.08 K to 0.92 K. The first panel is identical to Figure 1b. The critical state model of Ref. [5] appears to qualitatively describe the I_C behaviour up to higher temperatures very well. The range of the Meissner regime decreases with increasing temperature. As the range of the Meissner regime shrinks in field, the vortex flow regime (red) begins to appear at lower field but never at zero field. Using these measurements, we extract Λ at various temperatures, as presented in Figure 1d.

I_C and I_R vs temperature

It can be seen from Figure 9 that the critical current I_C changes significantly from 0.08 K to 0.92 K, however in the same range of temperatures, the retrapping current I_R changes very little. This suggests that whilst the device is undergoing dissipation at the mV scale, the local temperature is significantly higher than the measured temperature.

Retrapping in the flux flow regime

The curves in Figure 4a,b are measured at elevated temperatures, $T > 240$ mK. At lower temperatures, the nucleation or depinning rate of vortices is suppressed, and the low-voltage curves become stochastic, as shown in Figure 10a. Here, we show 35 upward sweeps from $1.6\mu A$ to $2.2\mu A$. Upon successive sweeps, the voltage jumps from the sub- μV level to the few- μV range at different values of the current. Upon ramping the current down, the retrapping occurs at a lower value of current, Figure 10b. Note that this switching and retrapping behavior is similar to that shown in Figure 1e,f. The difference is that here the switching brings the system to the vortex flow regime rather than the normal state of Figure 4a.

Zero-field Switching Current Heatmap

In Figure 11 we plot a bias-field map of the voltage in device B, plotted on a logarithmic colour scale and for an expanded range of field. It can be seen from the map that the vortex flow regime (light blue) does not appear until at positive field until 12 mT.

Zero-field Switching Current Heatmap

Measurements of the distribution of switching currents at zero-field and a range of temperatures is presented in

Figure 12. The histograms presented in Figure 2 correspond to cuts in Figure 12. The distribution remains unimodal across all temperatures, with the mean decreasing with increasing temperature.

Zero-field Switching IV-Curves

IV curves displaying individual switching events of the device B are presented in Figure 13 at a range of temperatures. It can be seen that the μV scale dissipation, which we associate with vortex flow, is not present even at higher temperatures, up to at least 0.71 K.

Switching Current Heatmap at 6.3 mT

Measurements of the distribution of switching currents at 6.3 mT and a range of temperatures is presented in Figure 14. It can be seen that the double-peak structure evolves non-trivially with temperature. As the temperature increases, the peaks appear to merge, resulting in one dominant peak. If we interpret the histogram as two independent distributions summed, it could also be the case that one of these distributions dominates over the other. In this case the distribution with a larger mean I_{SW} dominates at higher temperatures. Note that the temperature steps are uneven, meaning that some of the histograms appear elongated in the x-direction.

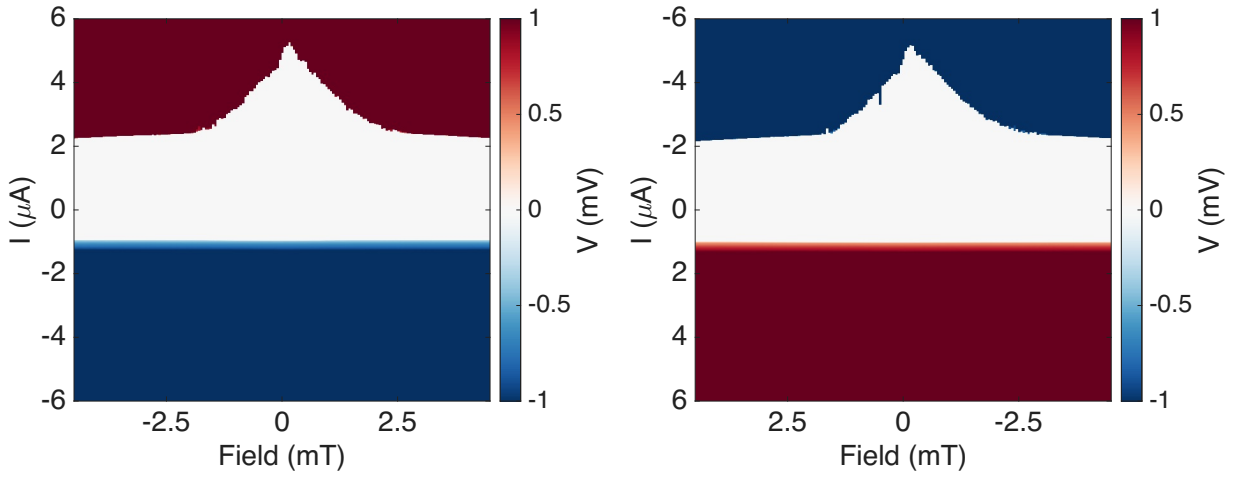


FIG. 5. Measured voltages in the device presented in Figures 1 and 4 at 0.08 K. The left (right) plot displays the voltage as the current is swept from negative (positive) to positive (negative). On the right plot, the x and y axis have both been flipped.

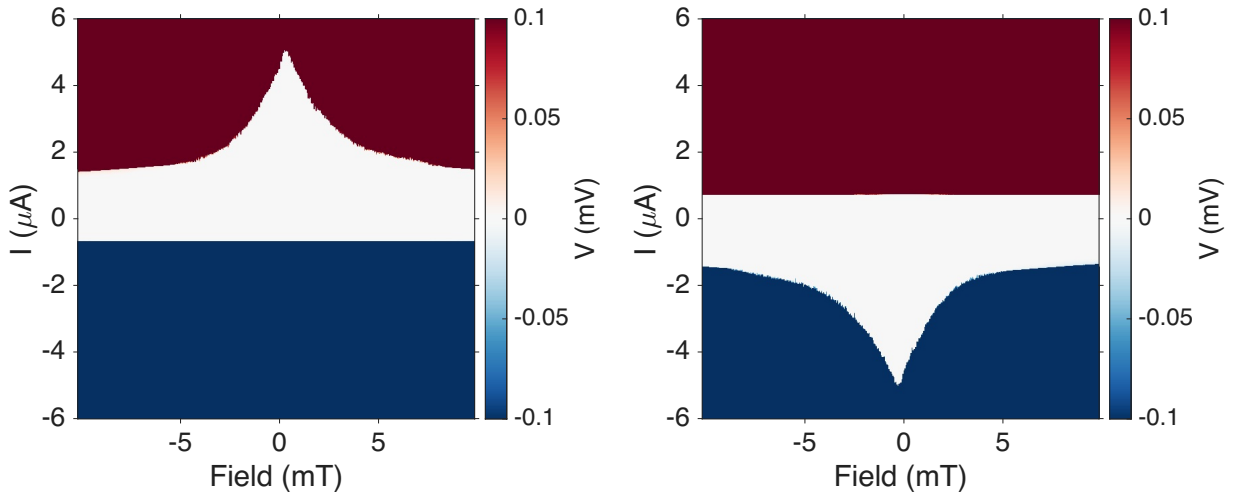


FIG. 6. Bias-field maps of measured voltage in the device B, as presented in Figure 2 and Figure 3. The left plot displays the voltage on an upwards sweep on a logarithmic scale. Upwards and negative sweeps of bias are shown in the middle and right plots respectively.

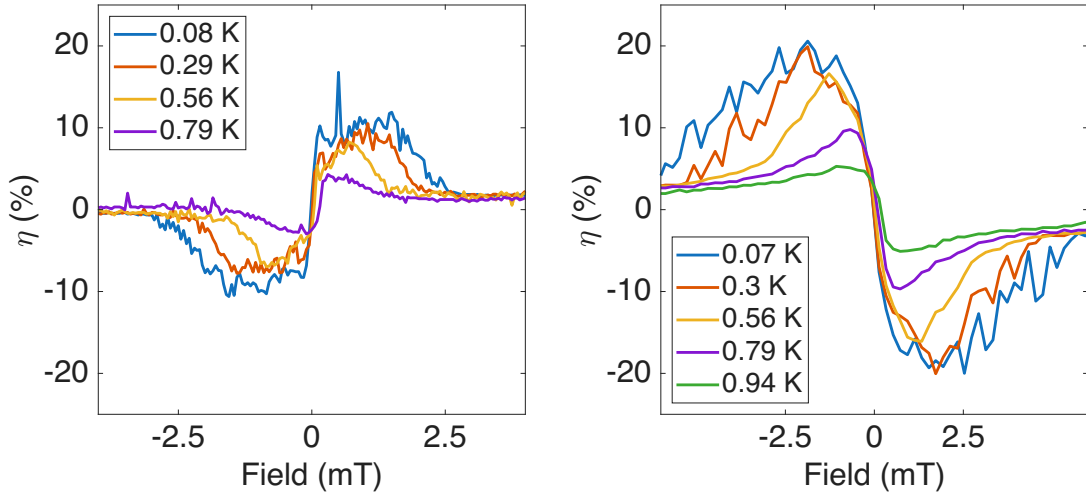


FIG. 7. Superconducting diode efficiency (η) extracted directly from Figure 5 and at various temperatures (left). The right plot displays another device with a greater surface barrier asymmetry, and as a result a larger diode efficiency.

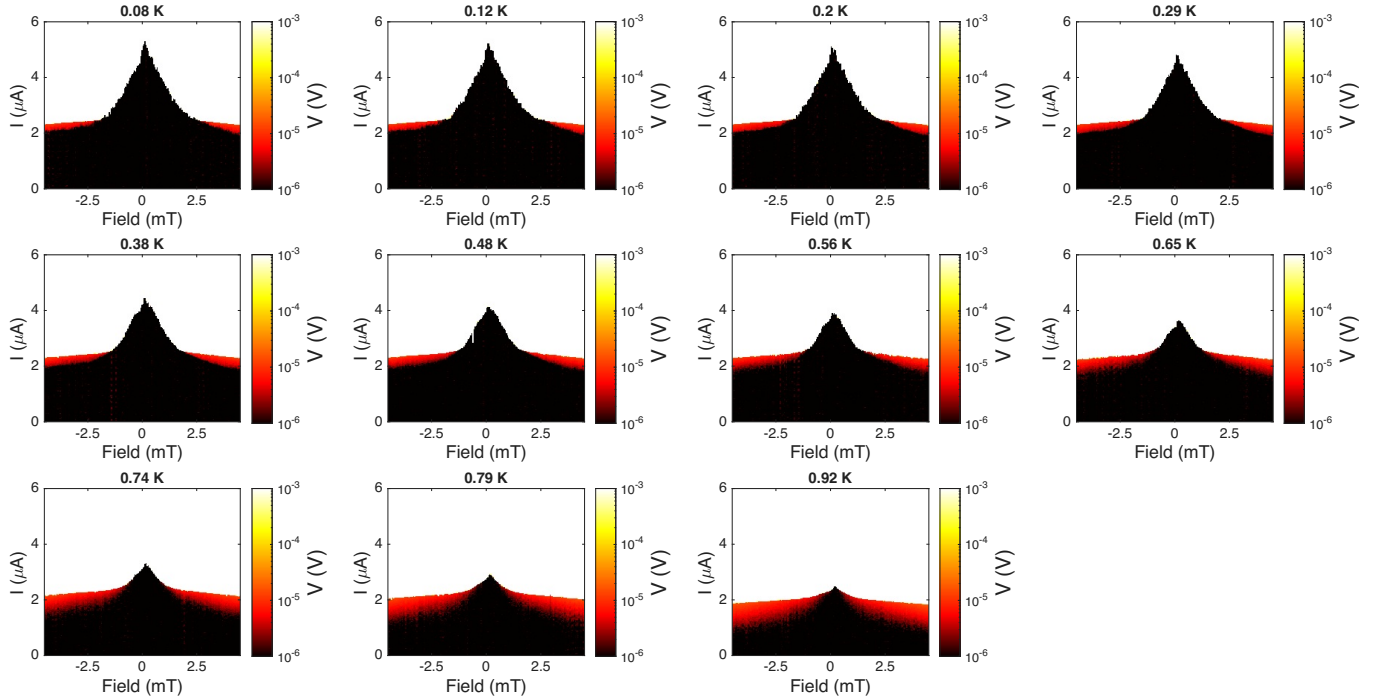


FIG. 8. Measured voltages in the device presented in Figures 1 and 4 at various temperatures.

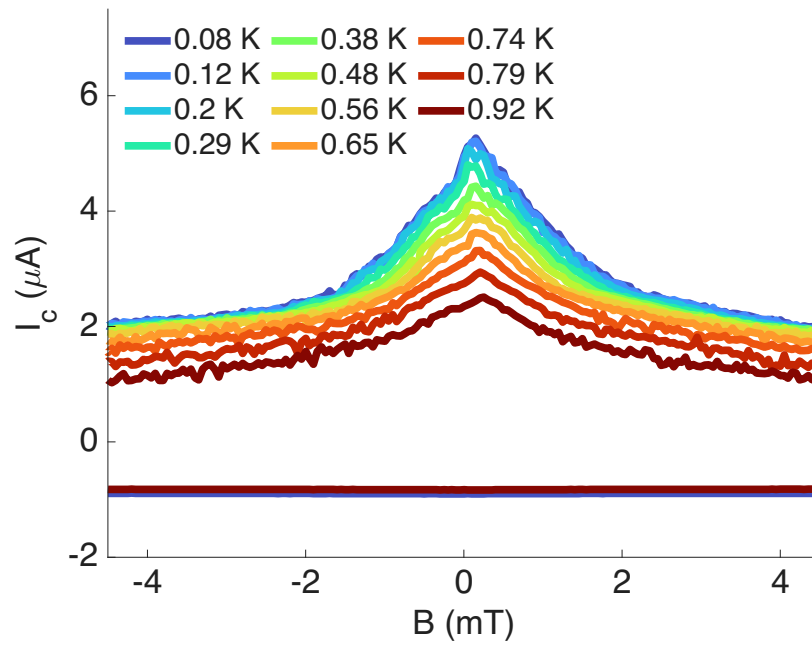


FIG. 9. Critical current and retrapping current at various temperatures in the device A.

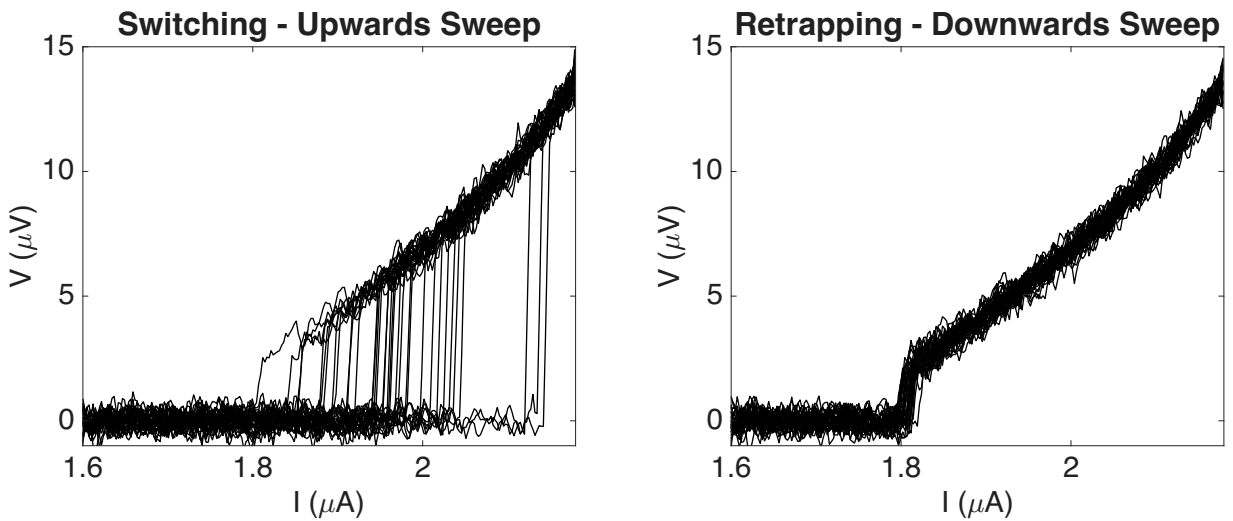


FIG. 10. Upwards and downwards sweeps of bias at 5.6 mT and 0.07K, repeated 35 times.

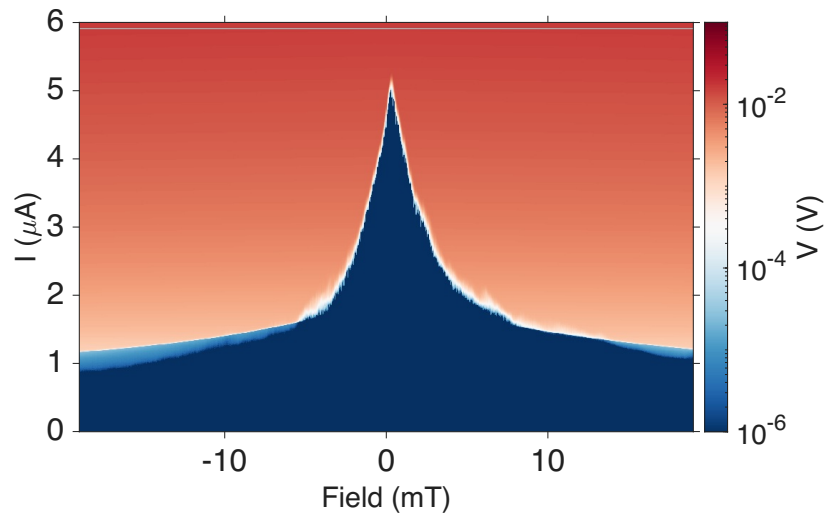


FIG. 11. Bias-field map of voltage in device B, plotted on a logarithmic colour scale.

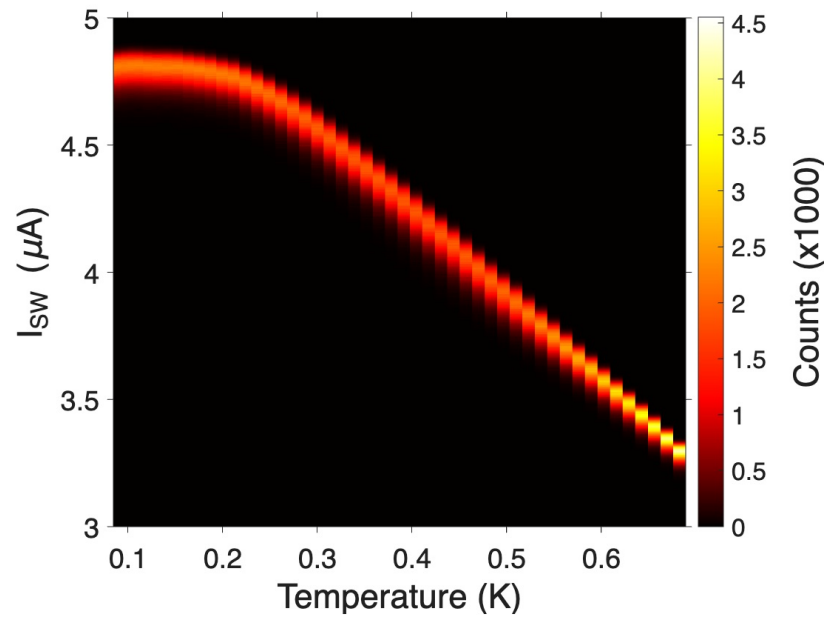


FIG. 12. Heatmap of switching currents at zero field, corresponding to measurements presented in Figure 2.

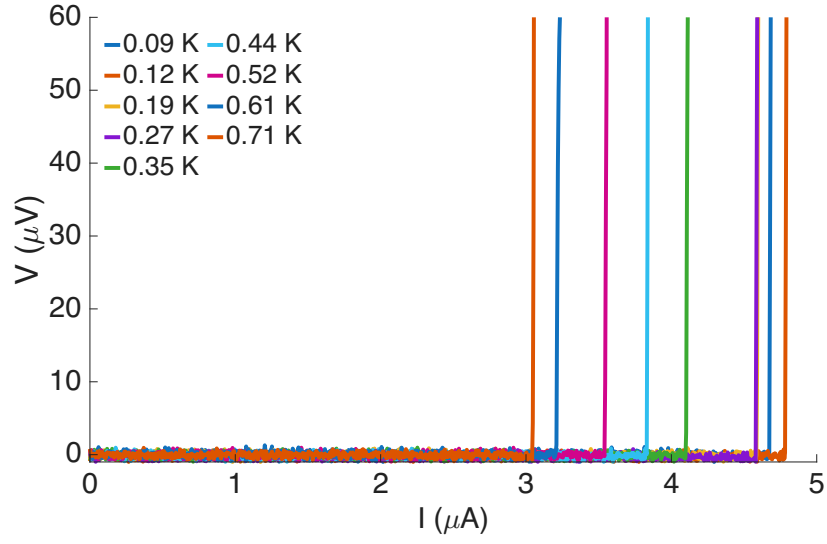


FIG. 13. IV curves displaying individual switching events of the device presented in Figure 2 and Figure 3

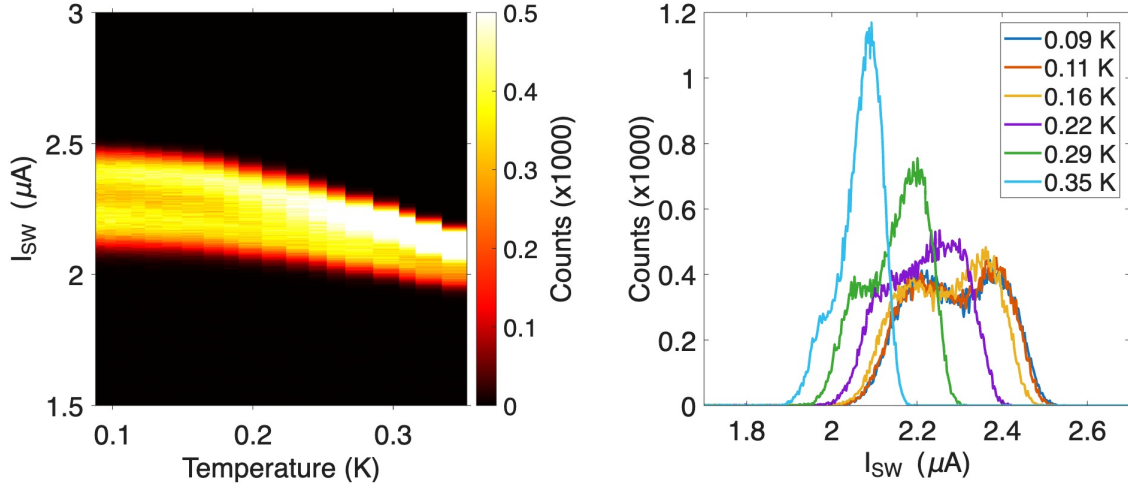


FIG. 14. Heatmap of switching currents at 6.3 mT, corresponding to measurements presented in Figure 3. Cuts at various temperatures are also presented (right). Note that the colourbar has been capped in order to accentuate the double-peak structure at low temperatures.